IEEE Access
Multidisciplinary | Rapid Review | Open Access Journal

Received February 25, 2020, accepted March 2, 2020, date of publication March 9, 2020, date of current version March 17, 2020.

Digital Object Identifier 10.1109/ACCESS.2020.2979291

Multi-Temporal Landsat Data Automatic Cloud Removal Using Poisson Blending

CHANGMIAO HU, LIAN-ZHI HUO, ZHENG ZHANG, AND PING TANG
Aerospace Information Research Institute, Chinese Academy of Sciences, Beijing 100101, China

Corresponding author: Lian-Zhi Huo (huolz@aircas.ac.cn)

This work was supported in part by the National Natural Science Foundation of China under Grant 41601384, Grant 41971396, Grant 41701399, and Grant 41401421, and in part by the Strategic Priority Research Program of the Chinese Academy of Sciences under Grant XDA19080301.

ABSTRACT Cloud and cloud shadow are common issues in optical satellite imagery, which greatly reduce the usage of data archive. As for the Landsat data, great advances have been made on detecting cloud and cloud shadow. However, few studies were performed on Landsat cloud removal for large areas. To facilitate land cover dynamics studies with high temporal resolution, we present an automatic cloud removal algorithm in this paper. Specifically, For Landsat Collection 1 Level-1 surface reflectance products, the algorithm first builds a cloud mask from the Quality Assessment (QA) band, and then reconstructs cloud-contaminated portions based on multi-temporal Landsat images with temporal similarity. To further eliminate radiation differences between cloud-free and reconstructed regions, a Poisson blending algorithm is adopted. Besides, the efficiency of gradient-domain compositing is accelerated by the quad-tree approach. Experiments have been performed to process more than 50,000 Landsat 8 Operational Land Imager (OLI) images covering China from 2013 to 2017, which yield promising results in terms of radiometric accuracy and consistency for experimental images with cloud coverage less than 80%. The produced Landsat time series images with cloud removal can be further used for analyzing land cover and land change dynamics in China, and the proposed algorithm should be easily employed to produce cloud-free Landsat time series for other areas.

INDEX TERMS Cloud removal, Landsat Collection 1, Poisson blending.

I. INTRODUCTION

Remote sensing imagery has been widely used for different applications, especially with recent advancements on machine learning algorithms [1]–[8]. Equipped with many advanced data analysis tools, we still face another great challenge in optical satellite image analysis: cloud. Cloud and cloud shadow are common issues in optical satellite imagery, which limit the power of optical images and increase the difficulty of time series analysis. Cloud detection and removal has always been an important issue in remote sensing image processing. Early cloud removal techniques are mainly based on single or small-scale images due to limited remote sensing data sources and limited cloud detection accuracy. With the development of remote sensing technology, especially the free-open policy of the Landsat data, a long data record spanning more than four decades are presented to all researchers over the world to monitor the Earth [9], [10]. However, cloud and cloud shadow hinder further processing of Landsat time series stacks. Hence, to produce cloud free Landsat time series data has become a research hotspot recently.

For Landsat data cloud removal study, a number of multi-temporal-based cloud removal algorithms have been proposed [14]–[17]. Gabarda and Cristóbal [14] introduced a cloud removal method based on image fusion that involves a 1-D pseudo-Wigner distribution transformation and a pixel-wise cloud model. Helmer and Ruefenacht [15] utilized regression tree to detect and predict pixel values underneath clouds and cloud shadows from other image data captured at different time. Lin *et al.* [16] proposed a nonlinear scheme instead of a linear one to mathematically formulate the reconstruction problem as a Poisson blending and then solved the equation using a global optimization process. Since Poisson blending is sensitive to boundary conditions, Lin *et al.* [17] further developed a patch-based scheme using temporal correlation: multi-temporal images were segmented into several patches with similar temporal variations; patches in the reference images were then sorted using the root mean squared error (RMSE) index to select cloning patches, and information of selected patches was seamlessly cloned to

The associate editor coordinating the review of this manuscript and approving it for publication was L. Zhang.

corresponding cloud-contaminated patches. The multi-patch information reconstruction was solved using an optimization process with the optimal seam. Although the patch-based algorithm [16], [17] can yield good cloud-free results, the whole process is complicated, which hinders its application to an automatic production line of large amounts of images. Another problem is how to achieve automatic detection of clouds and cloud shadows in Landsat images. Due to limited accuracy of the Landsat cloud cover assessment (CCA) algorithm, all cloud masks used in [14]–[17] depend on manual correction of existing cloud masks, which also hinders being equipped into an automatic processing line. From December 2017, USGS began to update Landsat product version form Pre-Collection to Collection 1 [12]. In the new version, the C version of the Function of Mask (CFMask) algorithm [18] replaces the older CCA algorithm to produce cloud, cloud confidence, cloud shadow, and snow/ice pixels [13]. The new Landsat product makes it possible to produce high-precision cloud & shadow masks automatically.

To achieve automatic cloud patching for large amounts of Landsat images efficiently and effectively, we propose an automatic cloud removal algorithm based on Poisson blending for multi-temporal Landsat data. The basic flow of the algorithm is: first, the cloud mask image is obtained automatically from Landsat Collection 1 Quality Assessment (QA) band data, and then modified by image morphology algorithm; second, thumbnails of original Landsat images are used to efficiently calculate the similarity among images, and further determine reference images patching order for each image; third, cloud patches are directly replaced by pixels according to the patch order; finally, for patch replacement images and replacement reference mask, the Poisson blending algorithm is used to eliminate the spectral difference of the patched area. Experiments were performed on more than 50,000 Landsat 8 images over China from 2013 to 2017. Experimental results have demonstrated that the proposed method can yield cloud-free Landsat image series in terms of radiometric accuracy and consistency.

Compared with previous studies, there are three major contributions in our paper: 1) the image thumbnails and cloud mask thumbnails are used to improve calculation speed in calculating the similarity and determine cloud patching reference images, enabling rapid processing of large amounts of data; 2) build a new cloud patching guidance vector for Poisson blending, and a box filter method is proposed for fast guidance vectors operation; and 3) to the best of our knowledge, this is the first study to perform automatic cloud removal for 5 years' Landsat time series at large scale (i.e., 527 Landsat WRS2 tiles covering China).

The rest of the paper is organized as follows: Section II describes the study area and data; Section III gives the proposed algorithm and also provides some illustrating figures; Section IV presents experimental results and discussions; and conclusion and future work are drawn in the final section.

II. STUDY AREA AND DATA

A. STUDY AREA

China is situated in East Asia, and its climate has distinct regional and seasonal characteristics due to East Asian Monsoon and complex topography. The topography varies greatly from Eastern to Western China, with an elevation ranging from −156 m to 8685 m above sea level.

B. DATA

In order to support China's land cover and land change mapping, we downloaded Landsat 8 OLI Collection 1 surface reflectance data from 2013 to 2017 from the USGS Earth Explorer. The surface reflectance data was produced based on the LaSRC algorithm [11]. This data include 527 Landsat WRS2 (Worldwide Reference System) path/row tiles, and in total more than 50,000 Landsat images, approximately 30TB in compressed packages in size.

The new Landsat Collection 1 data has three important improvements: 1) with higher level geometric accuracy suitable for pixel-level time series analysis; 2) improved the relative radiation consistency between different Landsat sensors (i.e., TM, ETM+ and OLI), and improved the accuracy of atmospheric correction; and 3) with a new version cloud/shadow mask based on the CFMask algorithm [18].

The CFMask algorithm populates cloud, cloud shadow, and snow/ice pixels in the processing of Landsat Level-1 data products, with the results represented as bit-mapped values within the Landsat Collection 1 Level-1 Quality Assessment (QA) Band. In short, CFMask is a multi-pass algorithm that uses decision trees to prospectively label pixels in the scene, and then validates or discards those labels according to scene-wide statistics. CFMask also creates a cloud shadow mask by iteratively estimating cloud heights and projecting them onto the ground [18].

III. METHODS

In this section, we present the proposed method in the following subsections: cloud mask extraction and modification, data resampling, calculating the similarity, determining cloud patching reference images, cloud patch direct replacement, and cloud patch Poisson blending. The flowchart of the proposed method can be found in the Fig. 1.

A. CLOUD MASK EXTRACTION AND MODIFICATION

The cloud mask image is obtained automatically from Landsat Collection 1 16-bit Quality Assessment (QA) band data, a new version 8-bit cloud mask (including cloud, cloud shadow, and high confidence cirrus) is created: the background is labeled as value 0, while the clear surface background as value 1, the cloud and High confidence cirrus as value 2, and the cloud shadow as value 3.

Although the CFMask algorithm achieves good detection performance, the cloud mask based on the QA band still has two limitations for our task: 1) some labeled pixels often appear too isolated, which is mainly caused by the fact that the

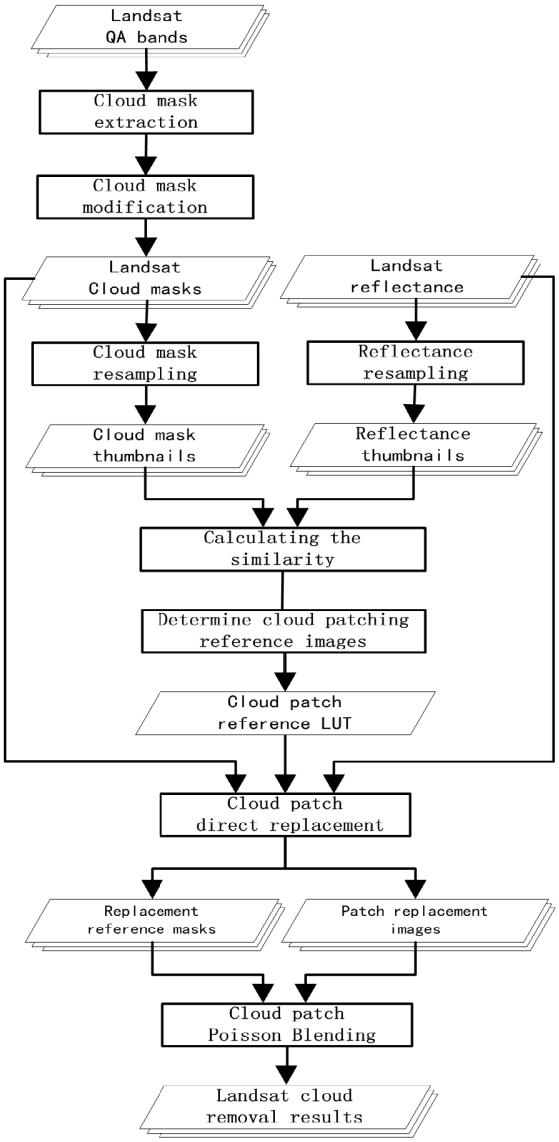

FIGURE 1. The flowchart of the proposed method.

CFMask algorithm uses decision trees to prospectively label pixels in the scene pixel-by-pixel, while ignoring positional relationships of adjacent pixels. However, an over-isolated cloud mask will reduce the quality and stability of subsequent cloud removal, and greatly increase computational complexity; and 2) the detection accuracy of CFMask at the cloud boundary, cloud shadow and haze boundary is not very high.

To solve the two problems above, especially considering automatic pipelines for processing a large number of data, a simple image morphology approach is proposed to modify cloud mask, which includes the following two steps: 1) reduce isolated pixels by a window filter: cloud and cloud shadow patches with less than 4 pixels in the cloud mask are re-labeled as value 1 (clear surface), and clear surface patches with less than 4 pixels are re-marked as 2 (cloud); and 2) dilate cloud and cloud shadow to extend the original mask's boundary, in which the cloud boundary is dilated by a radius of 5 pixels, while the less accurate cloud shadow boundary is dilated by a larger 10-pixel radius.

Compared with manual correction, the proposed cloud mask modification method is simple, robust and computationally fast, and can greatly improve the quality of the cloud mask. The original and modified cloud mask is shown in the Fig. 2.

B. DATA RESAMPLING

Using thumbnails instead of original size images in calculation is one of the key techniques of our algorithm. Since the cloud patching algorithm is based on multiple images, for each target image to be patched, some reference images need to be selected from all the images with the same path/row number. If the entire search process uses the original size images, program calculations will be extremely time consuming and even impossible for our task. Instead using thumbnails can significantly improve subsequent calculations of image similarity and determining cloud patching reference images. In more details, we resample the cloud mask to generate thumbnails by nearest neighbor interpolation method, and reduce the image to a quarter of its original size.

With the same idea as in the above subsection, reflectance data is also resampled to a quarter of its original size to calculate image similarities and determine cloud patching image order. For Landsat 8 OLI reflectance bands, only the band 2 (blue band, 0.450–0.515μm) is used to resample, which is significantly affected by atmosphere. In subsequent comparisons, only the blue-band thumbnails will be used to compare the similarities among all images.

C. CALCULATING THE SIMILARITY

In this step, image similarity is calculated for each image pair among the n Landsat images for the same path/row. The proposed similarity measure considers structural similarity (SSIM) index [16], image acquisition time difference and cloud cover rate in each image.

Let I_i, I_j be blue band thumbnail, and M_i, M_j be the corresponding cloud mask thumbnail, where $i, j \in n$. For the clear land surface area, mean values μ_i and μ_j, standard deviation values σ_i and σ_j, and covariance σ_{ij} are first computed. The SSIM value of I_i and I_j is defined as follows:

$$\mathrm{SSIM}(\mathrm{I}_i, \mathrm{I}_j) = \frac{(2\mu_i\mu_j + C)(2\sigma_{ij} + C)}{(\mu_i^2 + \mu_j^2 + C)(\sigma_i^2 + \sigma_j^2 + C)} \quad (1)$$

where C is a normalizing constant (e.g., $C = 2$). The larger the SSIM value, the more similar for the two corresponding images.

The image acquisition time is recorded in the auxiliary file of the Landsat surface reflectance product data. The acquisition difference date T_{ij} is defined as the number of days between acquisition dates for the two images I_i and I_j.

The amount of cloud cover is obtained by counting the number of cloud and cloud shadow pixels in the cloud mask thumbnails M_i and M_j.Let C_i and C_j be the cover amount of M_i and M_j separately, and C_{ij} is the cover amount in

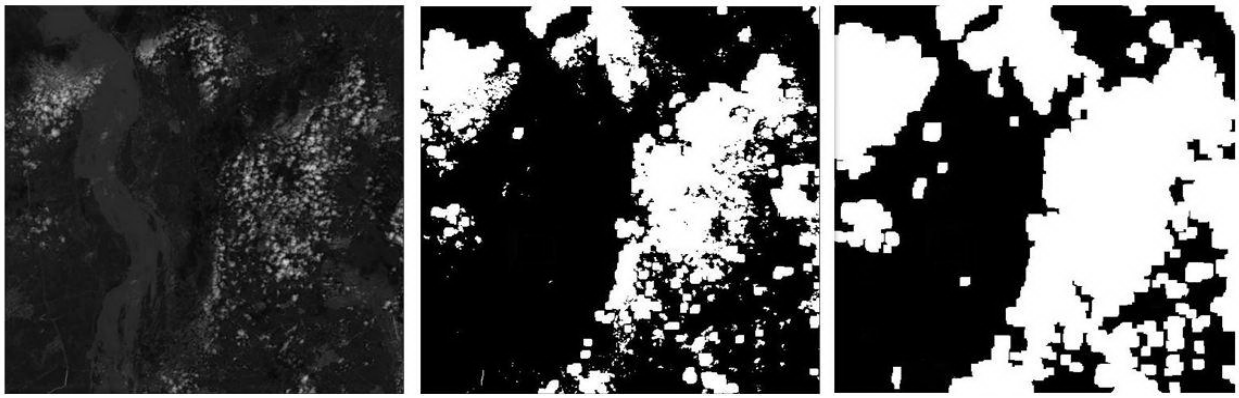

FIGURE 2. Illustration of the cloud mask modification. (Left) Original image. (Middle) CFMask's cloud mask. (Right) Result of two step image morphology modification.

both M_i and M_j at the same position. For the image I_i, the smaller the value C_j and C_{ij}, the more important the image I_j for cloud removal among reference image sequence.

Finally, for the target image I_i and one of the reference image I_j, the similarity calculation S_{ij} is defined as follows:

$$S_{ij} = a \times \mathrm{SSIM}(I_i, I_j) + b \times \frac{1}{T_{ij}} + c \times \frac{C_j + C_{ij}}{2M_{ij}} \quad (2)$$

where M_{ij} is the common non-zero pixel number in the cloud mask thumbnails M_i and M_j,including the non-background area (clear land surface, cloud and cloud shadow area), and a, b, c are constants, we empirically set all to 1 in the experiments. For I_i, the larger the value S_{ij} is, the more important the I_j is among the reference image sequence for the cloud removal task.

D. DETERMINING CLOUD PATCHING REFERENCE IMAGES

Once the similarity for each image pair in n images is identified, the next step is to obtain the sequence of reference images to replace the cloud-contaminated regions in the target image.

For each image I_i, the first reference image I_j is selected based on:

$$S_{ij}^{\max} = \max\{S_{ij}, i \neq j, j \in n\} \quad (3)$$

After obtaining the first reference image, scan all the cloud and cloud shadow areas in the I_i, and fill them with the I_j image if the corresponding geographic locations are clear land areas in the I_j; fill the left cloud and cloud shadow areas with the second similar reference image; repeat the above process until all the cloud area in the cloud mask M_i is patched; record the number of reference images used, patching order. The cloud patch reference lookup table records the number of reference images, file names, and patching sequences required for each Landsat image, and saves them as external text files.

Experiments found that due to the complexity of cloud detection results, some highlighted land surfaces were mis-labeled as clouds in the cloud mask of all images. In fact, there are very little images that can fill all the cloud areas in the cloud mask, and more are processed until the fill areas are no longer reduced. In most cases, the number of reference images required to repair an image does not exceed five.

E. CLOUD PATCH DIRECT REPLACEMENT

For each Landsat image of the same path and row number, the marked cloud and cloud shadow areas in the cloud mask are directly replaced by the clear land surface pixels from different reference images according to the patching order determined by the cloud patch reference lookup table. In this process, a replacement reference mask image is created to mark the source reference image of each replacement pixel. In the replacement mask image, the value i indicates that the patched pixel is from the i-th reference image, i ∈ [1,m], and m is the number of reference images. It is convenient to trace the patched area of each image and the patch source of each pixel.

Fig. 3(b) is an example of a replacement reference mask, where different gray levels within the patched area are from different reference images. Fig. 3(c) is an example of a cloud patch direct replacement. It can be seen that the direct replacement result has obvious visual radiation difference at different reference image boundaries within the repaired area boundary, so the subsequent cloud patch Poisson blending is needed to eliminate the radiation difference.

F. CLOUD PATCH POISSON BLENDING

Poisson blending is a concept of image editing presented by Pérez *et al.* [19], and widely used for seamless editing for high resolution aerial photography. In our cloud removal algorithm, the slightly different point is that the Poisson blending only needs to process pixel values of the repaired area and the boundary areas of different reference images in the repaired area. We first briefly summarize the principle of Poisson blending, as shown in the Fig. 4.

Let S be the image definition domain, and Ω be a closed subset of S with boundary $\partial\Omega$. Let f^* be a known scalar function defined over S minus the interior of Ω and let f be

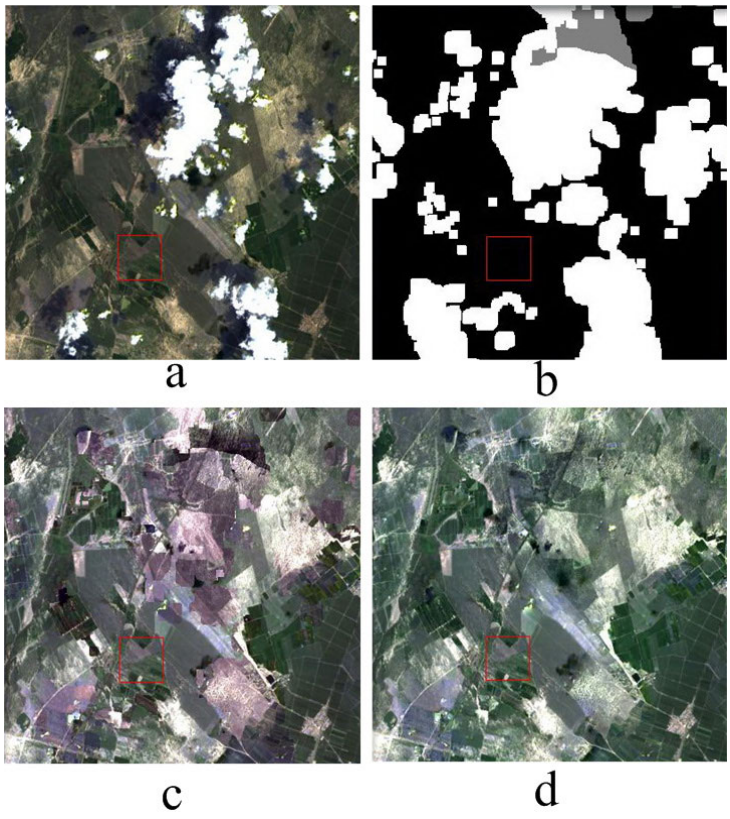

FIGURE 3. Cloud removal result. R:Band4, G:Band3, B:Band2. (a) Target image, and (b) replacement reference mask. Different colors in the mask region associated with different reference images. (c) Result of patch replacement, (d) result after Poisson blending.

an unknown scalar function defined over the interior of Ω. Finally, let V be a vector field defined over Ω. By introducing a constraint in the form of a guidance field V, the Poisson blending was proposed as follows [19].

$$\min \iint_{\Omega} |\nabla f - V|^2 \quad \text{with } f|_{\partial\Omega} = f^*|_{\partial\Omega} \tag{4}$$

whose solution is the unique solution of the following Poisson equation with Dirichlet boundary conditions:

$$\Delta f|_{\partial\Omega} = \text{div}V, \quad \text{with } f|_{\partial\Omega} = f^*|_{\partial\Omega} \tag{5}$$

where $\nabla\cdot = [\frac{\partial\cdot}{\partial x}, \frac{\partial\cdot}{\partial y}]$ is the gradient operator, and $\text{div}V = \frac{\partial u}{\partial x} + \frac{\partial v}{\partial y}$ is a divergence of $V = (u, v)$. When the guidance field V is conservative, i.e., it is the gradient of some function g, an alternative way to understand what Poisson blending does is to define the correction function $\tilde{f}$ on Ω such that $f^* = g + \tilde{f}$. The Poisson blending then becomes the following Laplace equation with boundary conditions:

$$\Delta\tilde{f}\Big|_{\Omega} = 0 \quad \text{over } \Omega, \quad \tilde{f}\,|_{\partial\Omega} = (f^* - g)\,|_{\partial\Omega} \tag{6}$$

Therefore, inside Ω, the additive correction $\tilde{f}$ is a membrane interpolant of the mismatch $(f^* - g)$ between the source and the destination along the boundary $\partial\Omega$. This particular instance of guided interpolation is used for seamless cloning [19].

As we can see that, the guidance vector field V is greatly important in the Poisson blending process. To have a better modeling capability, we define a new process calculation of guidance vector field V, which is different from the method in [16]. Considering there are two different types of pixel boundaries (i.e., patch area boundary $\partial\Omega$ and boundary between different reference images inside Ω), the guidance vector field V is separately calculated as follows: the value of V on $\partial\Omega$ and Ω without different reference images' boundaries is obtained using a common Laplacian convolution filter with four or eight connected neighbors of pixel. For the four neighborhood, the V value calculation formula is:

$$\begin{aligned} V(x, y) = {} & g(x+1, y) + g(x, y+1) \\ & + g(x-1, y) + g(x, y-1) - 4 \times g(x, y) \end{aligned} \tag{7}$$

While for the eight neighborhood, the formula is:

$$\begin{aligned} V(x, y) = {} & g(x+1, y) + g(x, y+1) + g(x-1, y) \\ & + g(x, y-1) + g(x+1, y+1) + g(x-1, y+1) \\ & + g(x+1, y-1) + g(x-1, y-1) - 8 \times g(x, y) \end{aligned} \tag{8}$$

For boundary between different reference images inside Ω (shown in the Fig. 4), the V value calculation uses only neighboring pixels from the same reference image. For example,

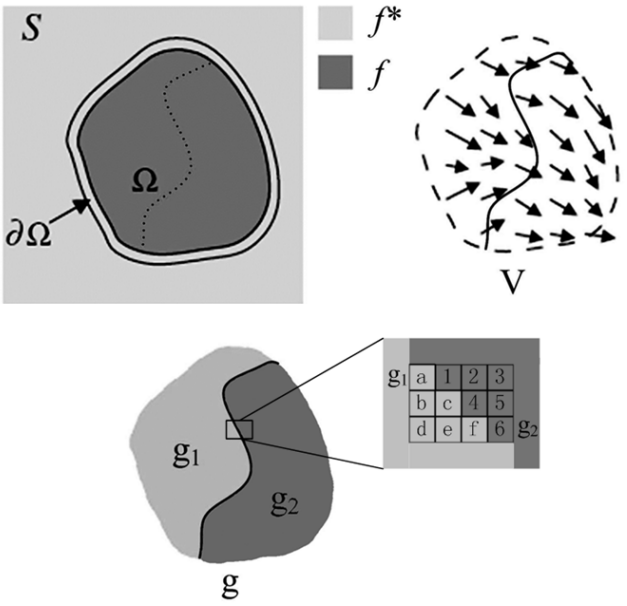

FIGURE 4. Illustration of the Poisson blending. The patch replacement image is the target image S, The cloud contaminated region in the target image S is denoted as Ω, and its boundary is denoted as ∂Ω. Let f be an unknown image intensity function defined over Ω. Let f* be the image intensity function defined over S minus Ω, and let V be a guidance vector field defined over Ω. Let g be the patched area pixel value function obtained by direct replacement, where g_1 and g_2 from different reference images.

with four neighborhood, the V values at pixel c of g_1 and pixel 4 of g_2 in the Fig. 4 are separately obtained by:

$$V(c) = g_1(b) + g_1(e) - 2 \times g_1(c) \tag{9}$$

$$V(4) = g_2(2) + g_2(5) - 2 \times g_2(4) \tag{10}$$

While with eight neighbors, the formula is corresponding turned into:

$$V(c) = g_1(a)+g_1(b)+g_1(d)+g_1(e)+g_1(f)-5 \times g_1(c) \tag{11}$$

$$V(4) = g_2(1)+g_2(2)+g_2(3)+g_2(5)+g_2(6) - 5 \times g_2(4) \tag{12}$$

By optimizing area boundary above, our algorithm generates a smooth guidance field. A smooth guidance field is very important for keeping the land surface spectral characteristics of the patched area, and conducive to the subsequent remote sensing classification research. By solving the Poisson equation with the obtained guidance vector field V, the new values are re-calculated and filled in the cloud and cloud shadow areas of each Landsat image.

Our algorithm was implemented in C++, with GDAL serving as the raster image reading and writing interface. Our tests were run on a desktop PC, with Intel Core i7-4610M CPU double 3.0-GHz CPU and 4-GB memory, and the operating system is the 64-bit Windows 7.

IV. EXPERIMENTAL RESULTS AND DISCUSSION

A. RADIOMETRIC CONSISTENCY ASSESSMENT

Radiometric consistency, or the quality of the final Poisson blending result quality, has already been discussed in Lin's papers [16], [17]. Compared with patch replacement, radiometric correction and boundary blending methods [21]–[23], Poisson blending method yields a better result in terms of radiometric consistency. Following Lin's experimental settings [16], [17], an experiment was conducted to quantify the accuracy and to compare with the Lin's cloud removal approach.

The experimental procedure was performed as follows: select a sequence of images that covers several different landscapes; simulate clouds by partly obscuring a cloud-free image of the sequence, and then compare the patched image with the original cloud-free image. A simulation image (Fig. 5) containing three simulated cloud-contaminated regions was tested. From visual inspection, the results generated by the two approaches have a similar radiometric consistency at the cloud boundaries. To further quantitatively compare the two approaches, root-mean-square error (RMSE), peak signal-to-noise ratio (PSNR), and SSIM index, are used to evaluate results, and the results are shown in the Table 1. In this experiment, two reference images were used: reference image Fig. 5 (b) has a better similarity with

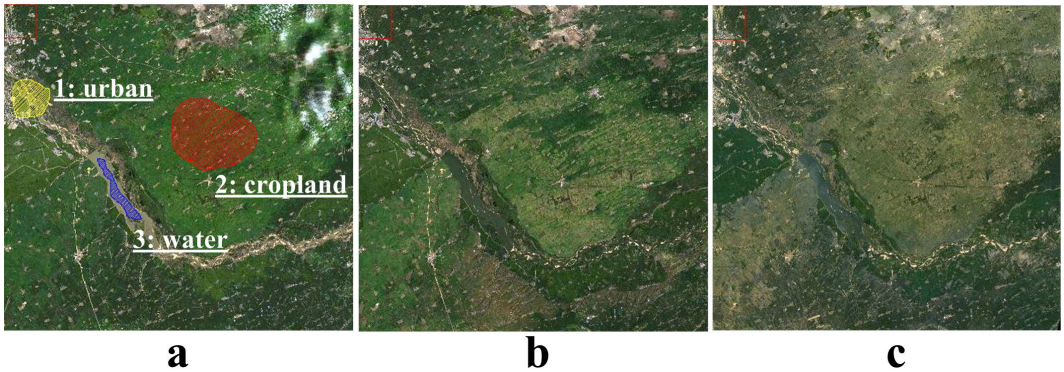

FIGURE 5. Simulation data. (a) Target image (2017/08/31) containing three simulated cloud-contaminated regions: 1 urban area with yellow mark (2372 pixels), 2 cropland area with red mark (9307 pixels), and 3 water area with blue mark (1061 pixels). (b) Reference image with similar month (2016/08/28). (c) Reference image with different month over 30 days (2015/07/09).

TABLE 1. Reconstruction accuracy by different approaches: A, patch replacement; B, radiometric correction with local color blending; C, Lin's approach [16]; and our approach. The simulation data a and the reference images b and c (denoted by ri_b and ri_c) shown in the Fig. 5 are used.

RMSE PSNR SSIM	1 urban area 2372 pixels ri_b / ri_c	2 cropland 9307 pixels ri_b / ri_c	3 water area 1061 pixels ri_b / ri_c
Approach A	7.110 / 8.013 30.32 /28.61 0.610 / 0.650	8.006 / 8.661 28.85 / 25.33 0.570 / 0.510	4.272 / 5.086 36.83 / 35.27 0.810 / 0.710
Approach B	6.311 / 6.879 31.92 / 30.83 0.680 / 0.680	6.590 / 7.241 29.39 / 27.11 0.650 / 0.560	4.002 / 4.385 36.89 / 36.39 0.830 / 0.760
Approach C	5.322 / 5.872 32.50 / 31.13 0.720 / 0.670	5.960 / 6.201 29.83 / 28.26 0.660 / 0.620	3.322 / 3.701 38.64 / 37.99 0.840 / 0.800
Our approach	5.415 / 6.093 32.65 / 31.26 0.690 / 0.680	5.653 / 6.108 29.41 / 28.29 0.650 / 0.620	3.485 / 3.626 38.59 / 37.85 0.840 / 0.780

the target image Fig. 5 (a) than reference image Fig. 5(c). From the statistical table, it is apparent that the approaches using reference image Fig. 5 (b) have better reconstruction accuracy than those using reference image Fig. 5(c). From the table, our approach generally has a similar reconstruction accuracy compared with Lin's approach [16]. Our Poisson blending algorithm differs from Lin's in the following procures: guidance vector field calculation, and Poisson equation optimization solution. The experiment indicates that the two implementations of Poisson blending result in similar or comparable patching performances.

However, our approach has a great advantage in reducing computational complexity, which will be discussed in more details in the following section.

B. COMPUTATIONAL EFFICIENCY ANALYSIS

To solve Poisson equation with guidance vector field V, there are mainly two solutions: the direct solution algorithm and the optimized solution algorithm.

The direct solution algorithm relies on a simple Cholesky decomposition [24], and uses sparse matrix in the Eigen library to reduce storage space and achieve fast operations [25]. And the direct solution algorithm's accuracy is much stable. However, the main drawback of the direct solution algorithm is its poor calculating speed: computing an n pixel composite requires solving a linear system with n variables; solving such a large system quickly overwhelms the main memory of a standard computer when performed for multi-mega-pixel composites, which are very common for remote sensing images.

The optimized solution algorithm uses an efficient gradient-domain compositing based on quadtrees [20], [26]. This algorithm performs a gradient-domain compositing approximately by solving an $O(p)$ linear system, where p is the total length of the seams between image regions in the composite; for typical cases, p is $O(\sqrt{n})$. This reduction is achieved by transforming the problem into a space where much of the solution is smooth, and then utilizing the pattern of this smoothness to adaptively subdivide the problem

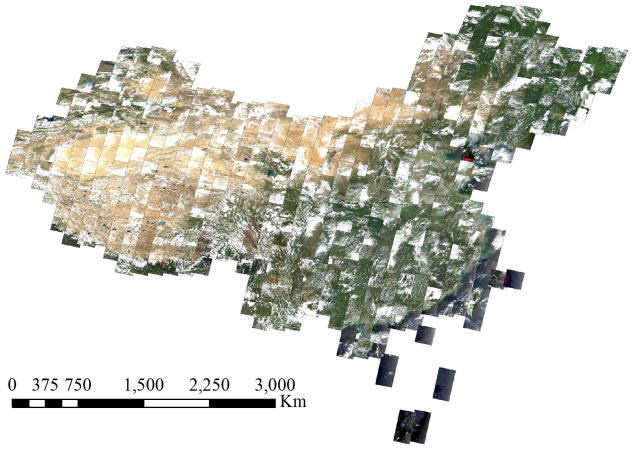

FIGURE 6. Original Landsat 8 image mosaics for China, captured in July, 2017. Image is shown according to the following rule: R: Band 4, G: Band 3, B: Band 2.

domain using quadtrees. This approach significantly reduces time and memory while achieving visually identical results.

For the above two algorithms, an test was performed to assess accuracy and calculation speed. 34 images with different cloud cover rates were used and the result was presented in the Table 2. The results show that the direct solution algorithm's accuracy is just slightly higher than that of the optimized solution algorithm, while the time consuming for the direct solution algorithm is nearly unacceptable when the cloud cover rate is over 30%.

TABLE 2. Poisson equation solving accuracy and calculating speed of cloud removal results generated by the direct solution algorithm (Alg_D) and optimized solution algorithm (Alg_O). 34 images with different cloud cover rates are used.

Cloud cover rate	<10% Alg_D / Alg_O	10%~20% Alg_D / Alg_O	20%~30% Alg_D / Alg_O
SSIM	0.858 / 0.857	0.808 / 0.812	0.752 / 0.750
Time (min)	0.2 / 0.8	1.2 / 1.0	4.3 / 1.6

30%~40% Alg_D / Alg_O	40%~50% Alg_D / Alg_O	50%~60% Alg_D / Alg_O	60%~80% Alg_D / Alg_O
0.661 / 0.661	0.637 / 0.610	0.606 / 0.581	0.551 / 0.547
10 / 1.8	23 / 2.2	48 / 2.3	>60 / 2.2

To take advantage of the two methods, we proposed a hybrid solution: we set a cloud cover rate threshold value as 30%; when the cloud cover rate for one Landsat tile is lower than the threshold, the direct solution algorithm is adopted, otherwise the optimized solution is employed. In this way, the accuracy of the results for whole China is maximally kept while the average processing time for each tile is confined within 5 minutes, which makes it possible to process a total 30TB dataset in an acceptable time.

In addition, the calculation of V on the boundary of different reference images inside Ω in Lin's approach [16] is much complicated: all the reference images need to be visited from hard disk files. Instead, our algorithm uses only two images: patch replacement image and replacement reference mask;

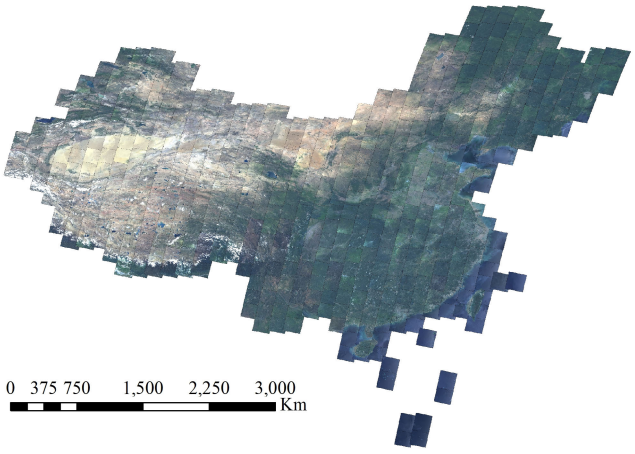

FIGURE 7. Landsat 8 image mosaics after cloud removal for China, captured in July, 2017. Image is shown according to the following rule: R: Band 4, G: Band 3, B: Band 2.

and the calculation speed of V is greatly accelerated by fast neighborhood window filtering operation, which is extremely important for the rapid processing of large amounts of images (e.g., considering the 30TB data in our case).

C. AUTOMATIC BATCH PROCESSING

For all the 50,000 files, the Landsat images with the same path/row number are placed in the same file folder, totally 527 folders to cover China.

Theoretically, our automatic cloud removal algorithm will process every image in one folder, and the derived result will be a dataset in which every image's cloud portions have been filled by other images. Actually, some Landsat data has a very high cloud cover even nearly 100%. For such data, it is hard to conduct the cloud patching completely, and even it doesn't make any sense for the results. Hence, in the processing pipeline, the data with a cloud cover greater than 80% is excluded from further processing.

A cloud removal result of fully covered China region can be found in Fig. 6 and Fig. 7. There are 527 images, which were captured in July, 2017. July is the most lush month for vegetation, and it is also the month with the most

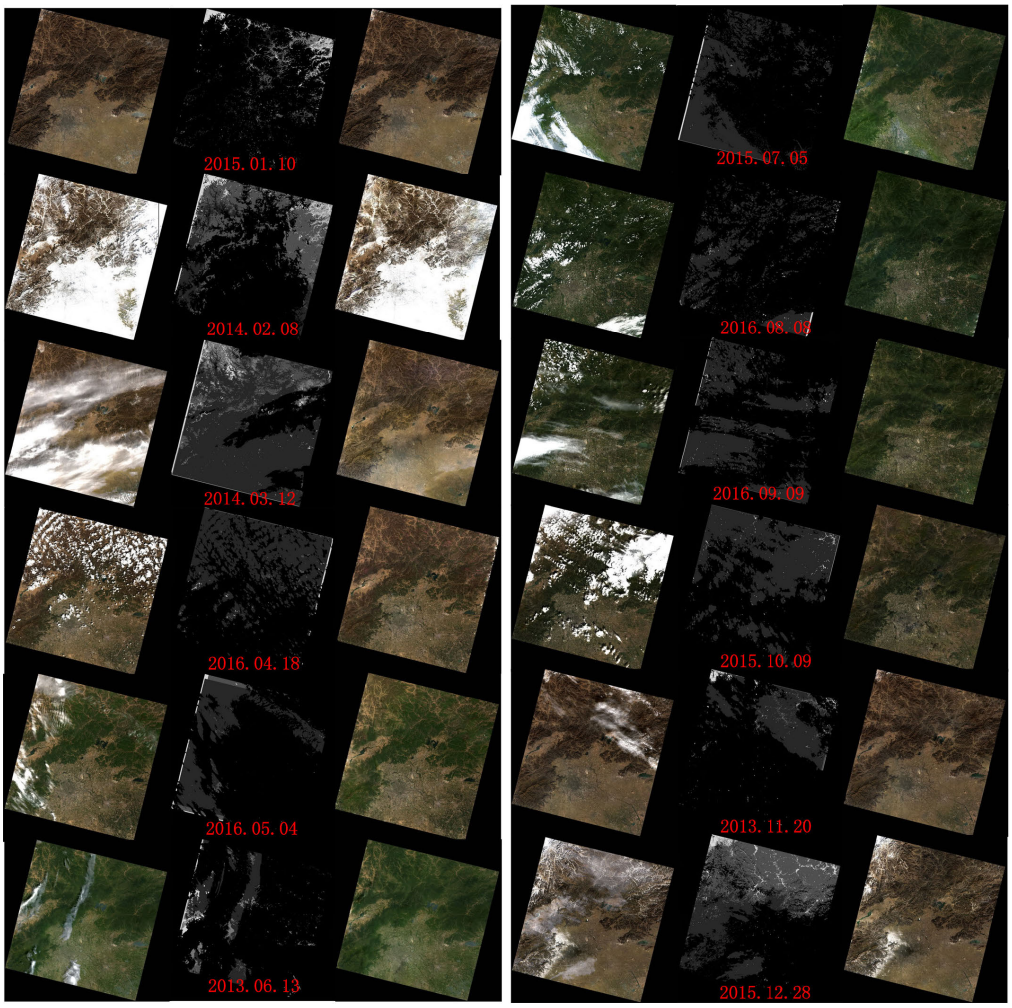

FIGURE 8. Cloud removal result. R:Band4, G:Band3, B:Band2. These images captured in WRS 2 path 119 row 029, near the northeast of China. (Left) Target image, (middle) cloud mask image, (Right) our result.

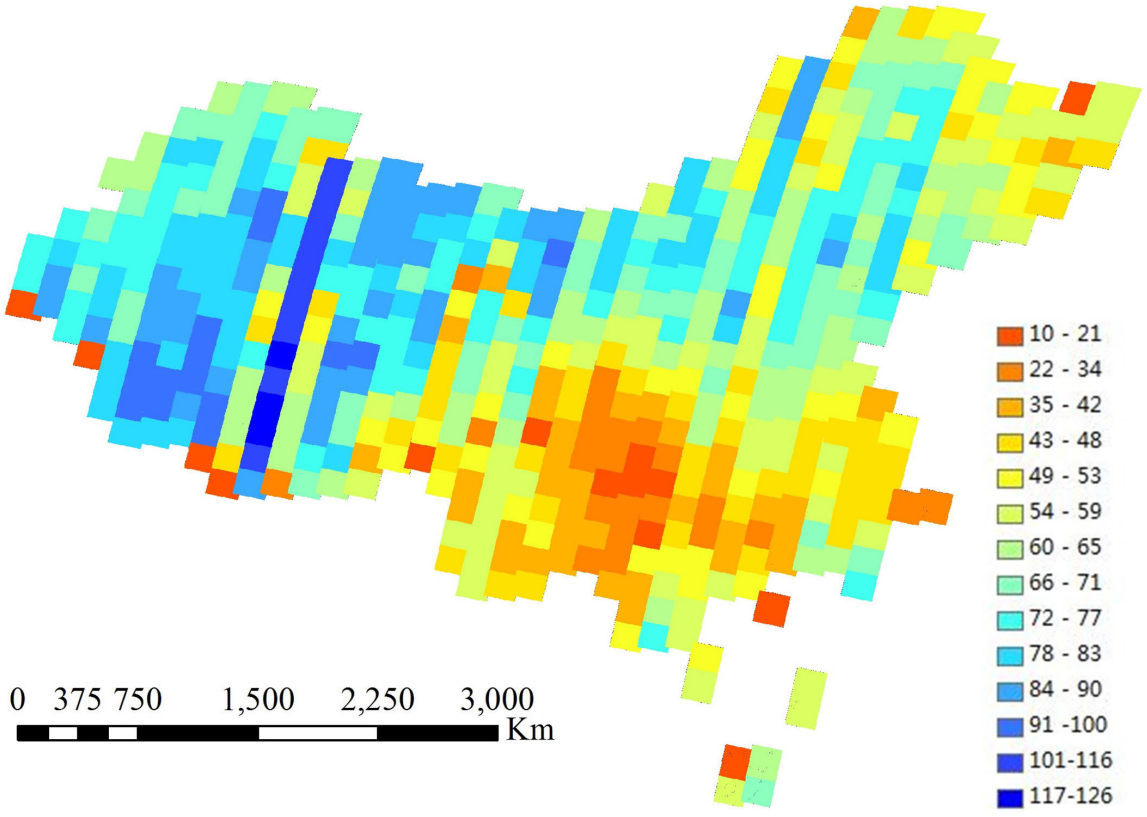

FIGURE 9. The number of finally obtained cloudless images in the five years' period for each tile over China.

abundant cloud. For most region of China, the number of cloud removal images with good quality in July is lower than in other months, especially in Southeast China. Based on our algorithm, a fully covered China, every 16 days (Landsat revisit cycle), one year (cloud patch area may come from a different year), cloudless dataset can be produced. The cloud removal process is fully automated, and only the poor quality result filtering is manual.

To have a better view of the temporal dimension of the produced data, we take one of the 527 areas as an example. The test images captured in the Landsat WRS2 tile path i119, row 029, near the northeast of China, from 2013 to 2017. There are a total of 82 images. After automatic batch processing, 65 images are cloud removed, and the remaining 17 images have a cloud and snow cover of greater than 80%. Not all the 65 images have good quality. By comparing the 65 result images before and after cloud removing manually, 5 images with poor quality are found. Finally, there are 60 images can be used as cloud removal result. We selected 14 images from 60 images, shown in the Fig. 8. The selected image were captured in different months. Although the cloud patch area may come from a different year, the trend of vegetation changes in a full year is fully revealed. We hope that this result can meet the needs of China's land cover classification research based on multi-temporal time series data.

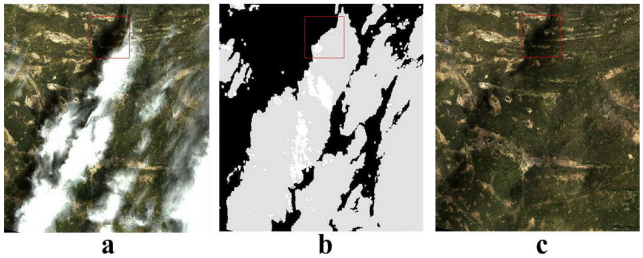

FIGURE 10. Error detection on cloud shadows. (a) Image visualized using bands 2–4 (2015/09/11). (b) Cloud mask based on CFMask with morphology modification. (c) Cloud removal result.

As for the produced 2013-2017 dataset for China, after filtering with 80% cloud cover and manually deleted removal images with poor quality (as detailed in the following subsection), the Fig. 9 shows that for each tile, the number of finally obtained cloudless images in five-year period. From the figure, we can see that for different regions, there are different numbers of available cloudless images; in general, the southwest of China has least good images. The figure also reflects the general cloud cover distribution over China for the five years.

D. LIMITATIONS

The performance of the proposed cloud removal algorithm highly relies on the quality of cloud and cloud shadow mask.

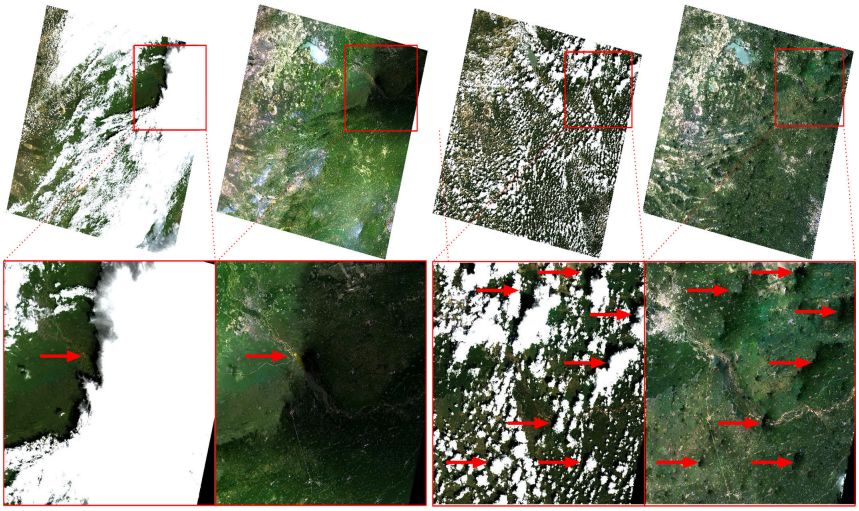

FIGURE 11. A low quality cloud removal result due to cloud shadow. R:Band4, G:Band3, B:Band2. Two images captured in WRS 2 path 119 row 029, near the northeast of China.

As mentioned in the last paragraph, 5 images with poor quality are found for the 119/029 tile. We examined the results and the results for other similar tiles, and found that the reason for the poor quality of removal result is mainly due to the low quality of cloud shadow marked by the CFMask algorithm (e.g., Fig. 10, Fig. 11). Compared to the cloud mask, the detection accuracy of cloud shadow by the CFMask is lower. Although achieving better results, image dilation operation adopted in the proposed algorithm cannot completely solve the issue. Hence, if the cloud and cloud shadow mask are incorrect, the performance of the proposed cloud removal algorithm greatly degrades.

V. CONCLUSION AND FUTURE WORK

In this paper, an automatic cloud removal algorithm for Landsat 8 data has been proposed. The cloud-contaminated portions of Landsat 8 Collection 1 surface reflectance image are first masked and removed automatically, and the missing pixels are reconstructed using multi-temporal Landsat images by estimating image similarity. By an efficient gradient-domain compositing algorithm using quad-trees, the Poisson blending can be computed in an efficient way. Experimental results on a sequence of images demonstrate that the proposed algorithm is very effective in reconstructing the cloud- and shadow-contaminated pixels with Landsat time series data. Based on our algorithm, a cloudless dataset with an interval of 16 days from 2013 to 2017, fully covering the whole China, has been automatically produced. To the best of our knowledge, this is the first cloud removed Landsat dataset for a large scale area (i.e., China) with five years' period and a high temporal interval. The dataset would greatly facilitate land cover dynamics studies with high temporal resolution in China.

Finally, we should stress that the success of the proposed algorithm heavily relies on a good cloud and shadow mask for Landsat data: if the CFMask algorithm fails to detect cloud patches, it will be nearly impossible for our algorithm to reconstruct the corresponding pixels. Although cloud detection results by the CFMask algorithm are satisfactory, there is much improvement space for shadow mask. To have a better reconstruction effect, a better shadow detection algorithm should be further studied.

REFERENCES

[1] M. Fauvel, Y. Tarabalka, J. A. Benediktsson, J. Chanussot, and J. C. Tilton, "Advances in spectral-spatial classification of hyperspectral images," *Proc. IEEE*, vol. 101, no. 3, pp. 652–675, Mar. 2013.

[2] L. Zhang, L. Zhang, and B. Du, "Deep learning for remote sensing data: A technical tutorial on the state of the art," *IEEE Geosci. Remote Sens. Mag.*, vol. 4, no. 2, pp. 22–40, Jun. 2016.

[3] L.-Z. Huo, P. Tang, Z. Zhang, and D. Tuia, "Semisupervised classification of remote sensing images with hierarchical spatial similarity," *IEEE Geosci. Remote Sens. Lett.*, vol. 12, no. 1, pp. 150–154, Jan. 2015.

[4] F. Luo, B. Du, L. Zhang, L. Zhang, and D. Tao, "Feature learning using spatial-spectral hypergraph discriminant analysis for hyperspectral image," *IEEE Trans. Cybern.*, vol. 49, no. 7, pp. 2406–2419, Jul. 2019.

[5] F. Luo, L. Zhang, X. Zhou, T. Guo, Y. Cheng, and T. Yin, "Sparse-adaptive hypergraph discriminant analysis for hyperspectral image classification," *IEEE Geosci. Remote Sens. Lett.*, to be published, doi: 10.1109/LGRS.2019.2936652.

[6] Z. Wang, B. Du, and Y. Guo, "Domain adaptation with neural embedding matching," *IEEE Trans. Neural Netw. Learn. Syst.*, to be published, doi: 10.1109/TNNLS.2019.2935608.

[7] Z. Liu, J. Wang, G. Liu, and L. Zhang, "Discriminative low-rank preserving projection for dimensionality reduction," *Appl. Soft Comput.*, vol. 85, Dec. 2019, Art. no. 105768.

[8] Z. Liu, Z. Lai, W. Ou, K. Zhang, and R. Zheng, "Structured optimal graph based sparse feature extraction for semi-supervised learning," *Signal Process.*, vol. 170, May 2020, Art. no. 107456.

[9] Z. Zhang, P. Tang, L. Huo, and Z. Zhou, "MODIS NDVI time series clustering under dynamic time warping," *Int. J. Wavelets, Multiresolution Inf. Process.*, vol. 12, no. 05, Sep. 2014, Art. no. 1461011.

[10] L.-Z. Huo, L. Boschetti, and A. Sparks, "Object-based classification of forest disturbance types in the conterminous united states," *Remote Sens.*, vol. 11, no. 5, p. 477, 2019.

[11] E. Vermote, C. Justice, M. Claverie, and B. Franch, "Preliminary analysis of the performance of the Landsat 8/OLI land surface reflectance product," *Remote Sens. Environ.*, vol. 185, pp. 46–56, Nov. 2016.

[12] USGS. (Oct. 2018). *Landsat 8 (L8) Data Users Handbook v3.0*. [Online]. Available: https://prd-wret.s3-us-west-2.amazonaws.com/assets/palladium/production/s3fs-public/atoms/files/LSDS-1574_L8_Data_Users_Handbook.pdf
[13] S. Foga, P. L. Scaramuzza, S. Guo, Z. Zhu, R. D. Dilley, T. Beckmann, G. L. Schmidt, J. L. Dwyer, M. Joseph Hughes, and B. Laue, "Cloud detection algorithm comparison and validation for operational landsat data products," *Remote Sens. Environ.*, vol. 194, pp. 379–390, Jun. 2017.
[14] S. Gabarda and G. Cristóbal, "Cloud covering denoising through image fusion," *Image Vis. Comput.*, vol. 25, no. 5, pp. 523–530, May 2007.
[15] E. H. Helmer and B. Ruefenacht, "Cloud-free satellite image mosaics with regression trees and histogram matching," *Photogramm. Eng. Remote Sens.*, vol. 71, no. 9, pp. 1079–1089, Sep. 2005.
[16] C.-H. Lin, P.-H. Tsai, K.-H. Lai, and J.-Y. Chen, "Cloud removal from multitemporal satellite images using information cloning," *IEEE Trans. Geosci. Remote Sens.*, vol. 51, no. 1, pp. 232–241, Jan. 2013.
[17] C.-H. Lin, K.-H. Lai, Z.-B. Chen, and J.-Y. Chen, "Patch-based information reconstruction of cloud-contaminated multitemporal images," *IEEE Trans. Geosci. Remote Sens.*, vol. 52, no. 1, pp. 163–174, Jan. 2014.
[18] Z. Zhu and C. E. Woodcock, "Object-based cloud and cloud shadow detection in Landsat imagery," *Remote Sens. Environ.*, vol. 118, pp. 83–94, Mar. 2012, doi: 10.1016/j.rse.2011.10.028.
[19] P. Pérez, M. Gangnet, and A. Blake, "Poisson image editing," in *Proc. SIGGRAPH ACM SIGGRAPH Papers*, 2003, pp. 313–318.
[20] A. Agarwala, "Efficient gradient-domain compositing using quadtrees," *ACM Trans. Graph.*, vol. 26, no. 3, p. 94, Jul. 2007.
[21] Q. Jiao, W. Luo, X. Liu, and B. Zhang, "Information reconstruction in the cloud removing area based on multi-temporal Chris images," *Proc. SPIE*, vol. 2007, Nov. 2007, Art. no. 679029.
[22] B. Wang, A. Ono, K. Muramatsu, and N. Fujiwara, "Automated detection and removal of clouds and their shadows from Landsat TM images," *IEICE Trans. Inf. Syst.*, vol. E82-D, no. 2, pp. 453–460, Feb. 1999.
[23] D.-C. Tseng, H.-T. Tseng, and C.-L. Chien, "Automatic cloud removal from multi-temporal SPOT images," *Appl. Math. Comput.*, vol. 205, no. 2, pp. 584–600, Nov. 2008.
[24] Rkaman. (2017). *Poisson_Blend—A Simple, Readable Implementation of Poisson Blending*. [Online]. Available: https://erkaman.github.io/posts/poisson_blending.html
[25] Eigen. *A C++ Template Library for Linear Algebra*. [Online]. Available: http://eigen.tuxfamily.org/index.php?title=Main_Page
[26] mkazhdan. (2018). *Adaptive Multigrid Solvers (Version 11.02): ImageStitching*. [Online]. Available: https://github.com/mkazhdan/PoissonRecon

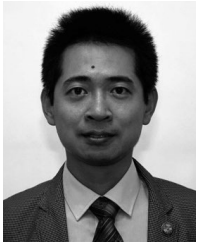

CHANGMIAO HU received the B.S. degree in mathematics from North China Electric Power University, Beijing, China, in 2006, and the Ph.D. degree in signal and information processing from the Institute of Remote Sensing Applications, Chinese Academy of Sciences, Beijing, in 2012. From 2012 to 2018, he was an Assistant Researcher with the Institute of Remote Sensing and Digital Earth, Chinese Academy of Sciences. He is currently working with the Aerospace Information Research Institute, Chinese Academy of Sciences. His research interests include remote sensing image processing, geometric correction, and atmospheric correction.

LIAN-ZHI HUO received the B.S. degree in geographic information system from Huazhong Agricultural University, Wuhan, China, in 2007, and the Ph.D. degree in signal and information processing from the Institute of Remote Sensing Applications, Chinese Academy of Sciences, Beijing, China, in 2012.

From 2012 to 2015, he was an Assistant Researcher with the Institute of Remote Sensing and Digital Earth, Chinese Academy of Sciences. From 2015 to 2018, he was a Postdoctoral Fellow with the University of Idaho, USA. He is currently working with the Aerospace Information Research Institute, Chinese Academy of Sciences. His research interests include image classification and machine learning.

Dr. Huo is reviewer for more than 15 international journals, including the IEEE TRANSACTIONS ON GEOSCIENCE AND REMOTE SENSING, IEEE JOURNAL OF SELECTED TOPICS IN APPLIED EARTH OBSERVATIONS IN REMOTE SENSING, IEEE GEOSCIENCE AND REMOTE SENSING LETTERS, and *Neurocomputing*.

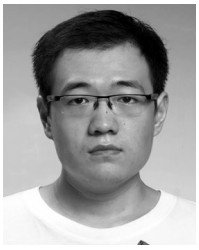

ZHENG ZHANG received the Ph.D. degree in signal and information processing from the Institute of Remote Sensing and Digital Earth, Chinese Academy of Sciences, Beijing, China, in 2016.

He is currently an Associate Professor with the Institute of Remote Sensing and Digital Earth, Chinese Academy of Sciences. His research interests include remote sensing image processing, time series analytics, deep learning, and artificial intelligence.

PING TANG received the Ph.D. degree in mathematics from Beijing Normal University, Beijing, China, in 1996. She spent two year as a Postdoctoral Researcher at the Institute of Geophysics, Chinese Academy of Sciences, Beijing. She is currently a Professor with the Aerospace Information Research Institute, Chinese Academy of Sciences. Her research interests include remote sensing image processing and applications, pattern classification, big data analytics.